Plasmonic Photothermal Heating of Intraperitoneal Tumors through the Use of an Implanted Near-Infrared Source

Alexander F. Bagley,[†,‡,§] Samuel Hill,[⊥] Gary S. Rogers,[⊥] and Sangeeta N. Bhatia[†,¶,#,▽,*]

[†]Koch Institute for Integrative Cancer Research, [¶]Health Sciences and Technology, and [#]Department of Electrical Engineering and Computer Science, Massachusetts Institute of Technology, Cambridge, Massachusetts, United States, [‡]Biophysics Program, Harvard University, Boston, Massachusetts, United States, [§]MD-PhD Program, Harvard Medical School, Boston, Massachusetts, United States, [⊥]Dermatologic Surgery & Oncology, Tufts University School of Medicine, Tufts Medical Center, Boston, MA, United States, and [▽]Howard Hughes Medical Institute, Chevy Chase, Maryland, United States

ABSTRACT Plasmonic nanomaterials including gold nanorods are effective agents for inducing heating in tumors. Because near-infrared (NIR) light has traditionally been delivered using extracorporeal sources, most applications of plasmonic photothermal therapy have focused on isolated subcutaneous tumors. For more complex models of disease such as advanced ovarian cancer, one of the primary barriers to gold nanorod-based strategies is the adequate delivery of NIR light to tumors located at varying depths within the body. To address this limitation, a series of implanted NIR illumination sources are described for the specific heating of gold nanorod-containing tissues. Through computational modeling and *ex vivo* studies, a candidate device is identified and validated in a model of orthotopic ovarian cancer. As the therapeutic, imaging, and diagnostic applications of plasmonic nanomaterials progress, effective methods for NIR light delivery to challenging anatomical regions will complement ongoing efforts to advance plasmonic photothermal therapy toward clinical use.

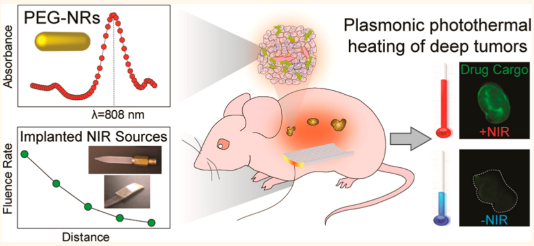

KEYWORDS: gold nanorods · implanted illumination · near-infrared · photothermal therapy · cancer

The unique optical and electromagnetic properties of plasmonic nanomaterials have generated interest in using these materials for a variety of applications in medicine ranging from clinical diagnostics and imaging to targeted tumor therapy.[1−5] The strong scattering and absorption properties of plasmonic nanomaterials have led to the development of highly sensitive plasmonic biosensors for detecting glucose from biofluids, epidermal growth factor receptors (EGFR) on human cancer cells, amyloid beta from blood, and cerebrospinal fluid in Alzheimer's Disease, and human papilloma virus DNA.[6−12] For therapeutic applications, the ability of plasmonic nanomaterials to absorb specific wavelengths of light and efficiently generate heat through the surface plasmon resonance (SPR) effect has been exploited for localized ablation of solid tumors, as well as for milder subablative heating to transiently damage nontumor endothelial cells or enhance delivery of therapeutic cargoes.[13−18] Collectively, these studies have demonstrated the potential for plasmonic photothermal therapy to impact a variety of pathophysiological processes such as tumor growth and angiogenesis. The advantages of polyethylene glycol-coated gold nanorods (PEG-NRs) in particular include their long-term stability, minimal cytotoxicity, and ability to be geometrically tuned to absorb specific wavelengths of NIR light.[16,17,19−23] In preclinical models, PEG-NRs passively accumulate in tumors, efficiently absorb NIR light, and generate localized heat through the SPR effect. To date, the therapeutic potential of PEG-NR-mediated photothermal ablation as well as subablative heating for recruitment of therapeutic cargoes has been demonstrated in both genetically engineered and xenograft animal models.[13,16,17,22−24]

One limitation of approaches involving NIR light delivered by an external device is the limited penetration depth of NIR light due to the optical absorption and scattering properties of biological tissue, which has restricted therapeutic studies to superficial tumors located near the skin surface.[25] For

* Address correspondence to sbhatia@mit.edu.

Received for review July 2, 2013 and accepted August 13, 2013.

10.1021/nn4033757

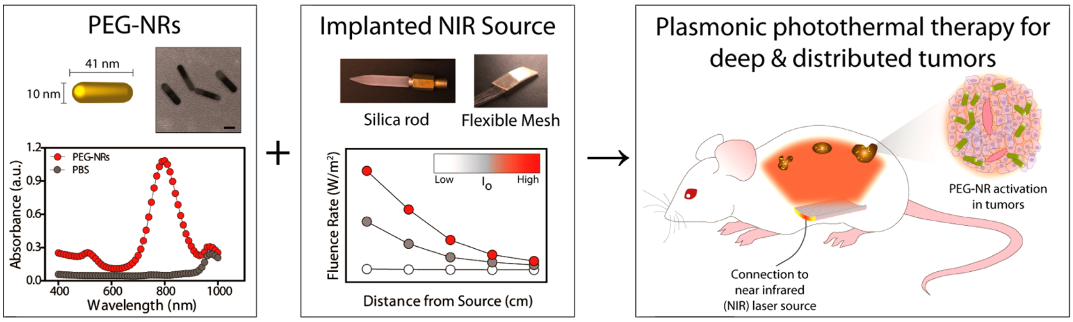

Figure 1. First component for plasmonic photothermal heating of intraperitoneal tumors consists of polyethylene glycol-coated gold nanorods (PEG-NRs), which are characterized by TEM imaging and optical absorbance. (Left panel) PEG-NRs with an aspect ratio of 4.1 display a peak surface plasmon resonance (SPR) at 808 nm. Scale bar: 20 nm. (Center panel) Classes of implanted NIR devices include silica rods and flexible meshes encased in silicone. Generalized fluence rate−distance relationship for several input currents (I_o) of an implanted NIR device. (Right panel) The combination of systemically administered PEG-NRs and implanted NIR illumination permits plasmonic photothermal therapy for intraperitoneal tumors.

solid tumors positioned in deeper, more anatomically challenging regions and distributed over larger areas, such as advanced ovarian cancer, it would be advantageous to have NIR light delivery systems capable of providing sufficient energy to elicit the SPR effect within these deeper and spatially distributed tumor environments. Several efforts to deliver light internally for applications such as photodynamic therapy have focused on optical fiber technologies, which direct a point source of light upon target tissues.[25−28] For laser-induced interstitial therapy (LITT) protocols, surface- and volume-scattering applicators have been developed to homogeneously scatter light after catheter-guided insertion directly into individual tumors.[29−31] By contrast, for scenarios requiring broader NIR illumination of multiple target tissues simultaneously, including tissues that may not be visible to the human eye or accessible by catheter, a source providing contiguous illumination over a larger surface area would be beneficial.

In this study, a potential strategy combining systemically delivered plasmonic nanomaterials with locally implanted NIR illumination sources is described. A series of biocompatible, implanted illumination devices are characterized through computational modeling, *ex vivo* fluence rate and thermographic measurements, and *in vivo* thermographic profiling. Two illumination devices were capable of heating solutions of PEG-NRs in a dose-dependent manner, and one of these devices was further validated by *in vivo* imaging and thermography. In animal models of orthotopic ovarian cancer pretreated with PEG-NRs, delivery of NIR light *via* the implanted device selectively elevated the temperature of ovarian tumors relative to background tissue without generating irreversible tissue damage and enhanced the delivery of diagnostic and therapeutic agents. Collectively, these data illustrate that synergies between plasmonic nanomaterials and novel NIR illumination methods can achieve selective and tolerable photothermal effects in complex anatomical environments.

RESULTS AND DISCUSSION

PEG-NRs were prepared from stock CTAB-coated gold nanorods to minimize toxicity and extend particle circulation time as previously described. (Figure 1, left)[16,17] Transmission electron microscopy (TEM) images revealed the PEG-NR dimensions to be 41 nm in length and 10 nm in width for an aspect ratio of 4.1 (Figure 1, left). The surface plasmon resonance (SPR) peak absorbance of PEG-NRs was 808 nm in accordance with previously observed measurements (Figure 1, left). Implanted NIR illumination devices were composed of silica rods and fiber optic meshes (Figure 1, center). Silica rods were designed with varying geometric parameters such as diameter, length, and tip tapering, treated to have uniform surface diffusivity along the rod, and joined with an SMA fiber-optic connector to interface with a continuous 810 nm NIR laser source. To provide a flexible alternative to the silica rods, fiber optic meshes consisting of submillimeter fibers encased in adhesive medical-grade silicone were prepared. Fibers were treated by an optomechanical scoring process prior to encasement to alter the total internal reflection at distinct locations and thereby permit NIR light emission along the length of the fibers. For each device, fluence rate−distance relationships were computed for input currents ranging from 9.0 to 13.0 A (Figure 1, center). The combination of systemic PEG-NRs and implanted NIR devices was investigated as a strategy to achieve photothermal heating in deep tumor nodules (Figure 1, right).

The abdominal cavity consists of organs and biological tissues with varying optical and geometric properties contained within a confined anatomical compartment. To develop a quantitative framework for understanding NIR illumination in the abdominal cavity and thereby assess the feasibility of the implanted NIR devices, a three-dimensional solid model incorporating the liver, spleen, stomach, kidney, large and small intestine, and skin was developed (Supporting Information, Figure 1, Figure 2a). For modeling simulations,

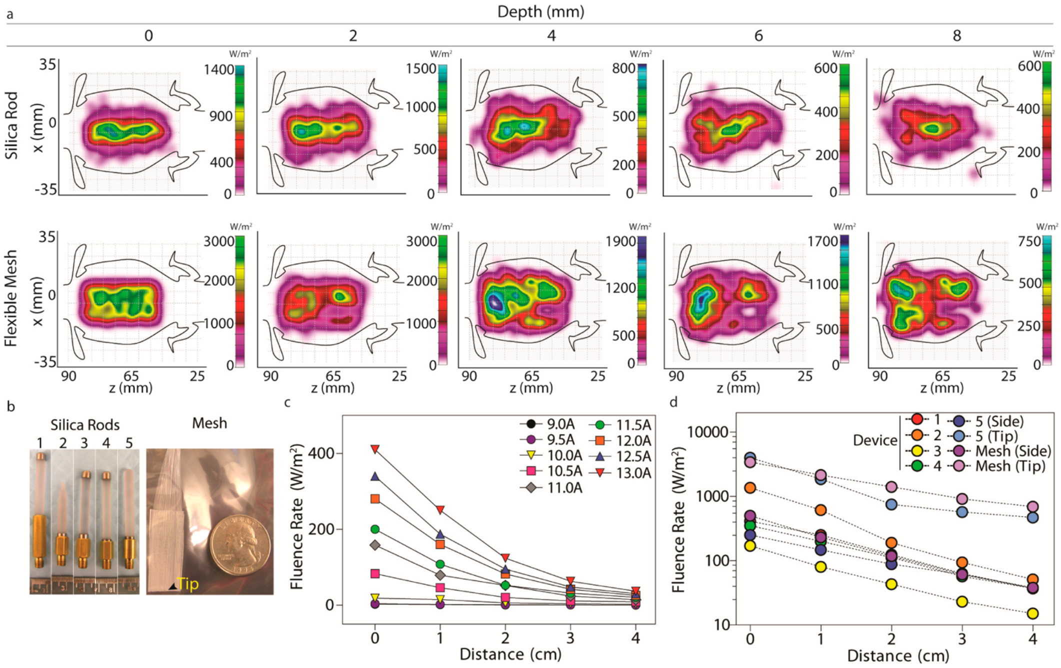

Figure 2. (a) Fluence rate simulation in the abdominal cavity with two implanted NIR devices at a length up to 8 mm depth from the skin surface. (b) Photographs of implanted NIR devices investigated include silica rods (devices 1–5) and mesh. (c) Fluence rates from a representative silica rod device for variable input currents ranging from 9.0 to 13.0 A and distances from source ranging from 0 to 4 cm. (d) Fluence rate–distance curves obtained at 13.0 A input current for multiple models (devices 1–5; mesh) and spatial orientations of implanted NIR devices.

abdominal organs were assigned approximate indices of refraction, scattering coefficients, and absorption coefficients based on values obtained from the literature (Supporting Information, Table 1). Previous computational models developed in our lab applied finite element simulations to approximate photothermal heating of gold nanorod-containing subcutaneous tumors using the bioheat transfer equation.[16] While the current model describes NIR light distribution in nontumor tissues within the abdominal cavity, future models incorporating tumor tissue elements, absorption coefficients dependent on gold nanorod tissue content, and biophysical heat transfer equations will be useful for providing a more detailed description of plasmonic photothermal heating in the abdominal cavity. The current deterministic model predicts that most of the emitted NIR light focuses on regions containing the intestine, liver, and spleen within the abdominal cavity with lambertian, or diffusely reflected, illumination along the silica rod (Figure 2a). In comparison, with a lambertian profile along the flexible mesh, the model predicts an enhanced, more uniform transmittance within the abdominal cavity due to increased surface area relative to the silica rod (Figure 2a). Importantly, simulations using this anatomically based model predicted the limitations of NIR light penetration due to tissue absorption and scattering. For example, at the interface of the silica rod and abdominal organs with an input power of 1 W along the device, the model predicts a peak fluence rate of 1.35×10^3 W/m^2, while at a distance 8 mm deep to the device, the peak fluence rate decays to 5.9×10^2 W/m^2 (Figure 2a). Similarly, at the interface of the flexible mesh and abdominal organs, the peak fluence rate is estimated to be 3.0×10^3 W/m^2, and the peak fluence rate decays to 7.3×10^2 W/m^2 at a depth of 8 mm (Figure 2a). The depth-dependent decay observed is consistent with tissue absorption and scattering and suggests that the model parameters approximate to a first order the *in vivo* environment.

To validate and refine model predictions for the silica rods and flexible mesh, fluence rate was calculated at multiple distances and input currents for six distinct implanted NIR devices (Figure 2b). Consistent with the model, fluence rate decreased approximately as the square of the distance between the device and detector plate when measured in an air medium (Figure 2c). As the input current from the laser was increased, a linear increase in fluence rate was observed at the surface of each implanted device, highlighting the ability to precisely tune the NIR emission from the devices to achieve the desired level of photothermal heating *in vivo* (Figure 2c). In contrast to the model predictions, the peak fluence rate measured for the flexible mesh surface (~500 W/m^2) did not reach the maximal surface fluence rate of 3.0×10^3 W/m^2 predicted by the model. Limitations related to the material properties and device fabrication likely contributed to the difference and suggest that future models could be refined by incorporating specific

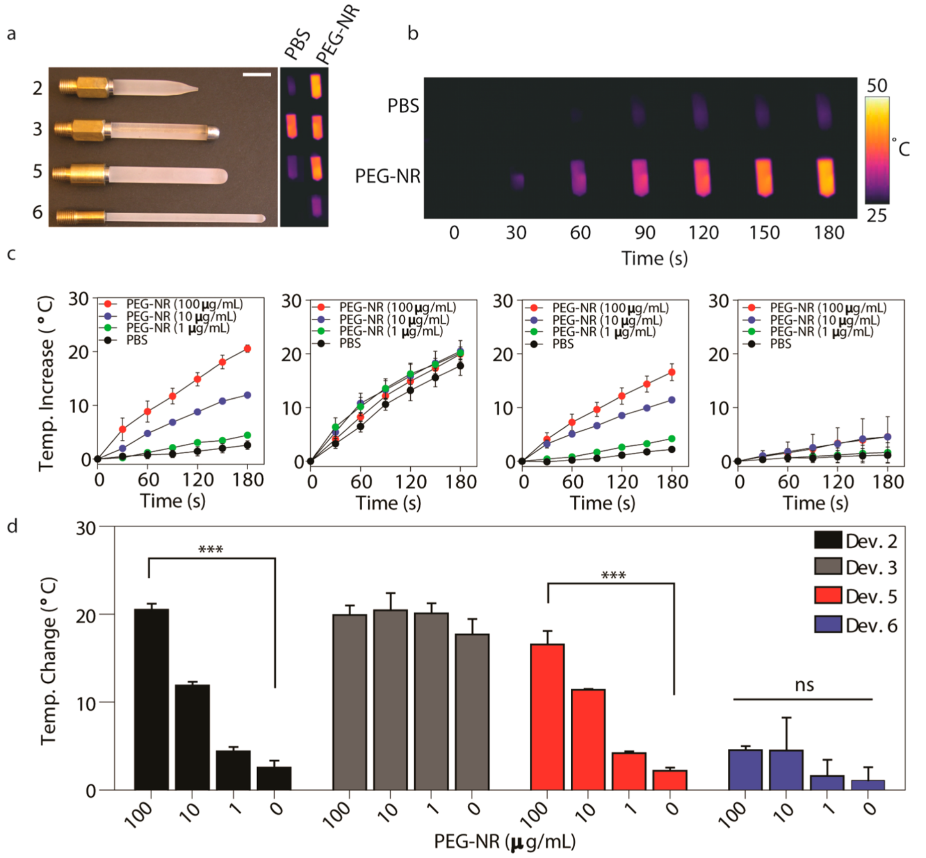

Figure 3. (a) Images of implanted NIR devices 2, 3, 5, and 6 (top to bottom). Infrared thermographic images of PEG-NR and PBS solutions after NIR exposure with implanted NIR devices. Scale bar: 1 cm. (b) Representative thermographic timecourse for device 2, illustrating selective heating of PEG-NRs. (c) PEG-NR heating for implanted NIR devices 2, 3, 5, and 6 (left to right) (*n* = 3 per group). Error bars, s.e.m. (d) Maximal temperature elevation for multiple PEG-NR concentrations. (*n* = 3 per group; ****P* < 0.001; one-way ANOVA and Tukey post-tests.) Error bars, s.e.m.

physical properties of the device in addition to tissue properties. Finally, surface fluence rate was highly dependent on the geometry of the device and spanned several orders of magnitude (4×10^3 W/m^2 to 2×10^{-1} W/m^2) (Figure 2d).

On the basis of the surface fluence rate measurements, we next assessed whether our devices possessed differing capacities to photothermally heat PEG-NRs. In an *ex vivo* setting, multiple concentrations of PEG-NRs in PBS were subjected to continuous NIR laser irradiation (810 nm) dispersed by each implanted device, and the temperature of PEG-NR solutions was continuously monitored *via* infrared thermography (Figure 3a,b). Several distinct patterns of photothermal heating were observed, which are denoted as (1) nonspecific, (2) PEG-NR-dependent, and (3) inefficient. Owing to elements of device construction that resulted in a greater localized concentration of laser energy at the device tip (device 3), nonspecific devices led to temperature elevations in both PEG-NR- and PBS control solutions (Figure 3c,d, Supporting Information, Figure 2). Conversely, devices with inefficient heating failed to yield an appreciable rise in temperature of PEG-NR solutions at approximately physiologic PEG-NR concentrations (Figure 3c,d, Supporting Information, Figure 2). A subset of implanted devices investigated, however, was observed to selectively elevate the temperature of PEG-NR solutions in a concentration-dependent manner while failing to significantly heat PBS control solutions (Figure 3c,d, Supporting Information, Figure 2). After 3 min of NIR irradiation, one PEG-NR-dependent heater (device 2) elevated a 100 μg/mL PEG-NR solution by 20.53 °C ± 0.68 °C, a 10 μg/mL PEG-NR solution by 11.90 °C ± 0.44 °C, a 1 μg/mL PEG-NR solution by 4.43 °C ± 0.47 °C, and a PBS control solution by 2.57 °C ± 0.79 °C. Collectively, this *ex vivo* characterization helped identify a subset of implanted NIR light sources to evaluate in an *in vivo* context.

The *ex vivo* fluence rate and PEG-NR photothermal heating measurements, coupled with computational models for two generic device geometries (i.e., silica rod and flexible mesh sheet) allowed for progressive down-selection of candidate devices prior to attempting plasmonic photothermal therapy in an animal model. Despite comparable fluence rate modeling predictions between the rod and mesh sheet, the various silica rod designs were pursued further because their material properties and construction proved able to sustain input powers in the anticipated range necessary for *in vivo* photothermal heating. The 6-fold lower measured surface fluence rate compared to the model prediction illustrated that incorporation of physical properties of the device would be advantageous for future simulations, and also that future iterations of the flexible mesh should include design parameters that can sustain the necessary power requirements for plasmonic photothermal heating.

Of the silica rod devices with the highest measured fluence rates, only a subset was able to heat PEG-NR solutions in a selective and dose-dependent manner. Those devices which failed to achieve PEG-NR-specific heating likely did so due to a combination of suboptimal geometric design and the incorporation of highly absorptive elements. Suboptimal geometries such as the long, narrow cylindrical design may have resulted in poorly diffused incoming NIR light with inhomogeneous emission to the surrounding environment. Such geometric constraints have been previously observed in the related field of laser-induced interstitial therapy, where NIR scattering from implanted laser applicators in part determines the volume of tissue susceptible to heating therapy.[32,33] While the power required for this ablative therapeutic modality is substantially higher than that required for plasmonic photothermal therapy, the ability of the implanted device to scatter NIR light isotropically and minimize heat conduction at the tissue-device interface is highly dependent on geometric and material design parameters and is important for ensuring broad tissue coverage. Incorporating a metallic cap at the device tip led to heating of both PEG-NR and control solutions nonselectively, suggesting that the metallic cap absorbed the incident NIR light to generate heat within the device itself. Such designs are not suitable for implantation into the abdominal cavity due to reduced, inhomogeneous light emission, as well as local coagulation of tissues in the vicinity of the device tip.[33] Limiting the incorporation of absorptive elements and improving light scattering from the device surface would help reduce the nonspecific heating observed here. The optimal implanted NIR device based on fluence rate and selective PEG-NR heating had a tapered tip design and a length of ~3 cm, which was among the shortest of the candidate devices investigated. Future iterations on silica- or fiber optic mesh-based implanted NIR devices will focus on improved flexibility, isotropic NIR emission from the device surface, and improved materials able to sustain a broader range of powers and thereby reduce the time required to reach the desired temperature range for plasmonic photothermal therapy.

The function of a silica rod from the PEG-NR-dependent activator group was next assessed in an orthotopic mouse model of ovarian cancer. The device was implanted into the abdominal cavity through an approximately 1 cm midline incision on the ventral surface and connected to the laser source *via* fiber optic cable (Figure 4a). To visualize the device inside the abdominal cavity, computed tomography (CT) imaging was performed. CT images clearly delineated the implanted device and revealed its placement relative to abdominal structures including intestine, abdominal wall, and vertebral bodies (Figure 4a, Supporting Information, Figure 3). To investigate the capability and specificity of the device to photothermally heat various tissues, the device was implanted into the abdominal cavity of animals pretreated with PEG-NRs or control animals lacking PEG-NRs, and the temperature of ovarian tumor tissue, intestine, and liver was continuously monitored with thermocouples placed at approximately equal distances (0.3−0.5 cm) from the implanted device within each of these tissues (Supporting Information, Figure 4). Thermal profiling revealed a more efficient heating process in ovarian tumors, intestines, and livers of PEG-NR-treated animals relative to control animals lacking PEG-NRs (Figure 4b−d). Modest temperature changes between 2.4 and 3.0 °C observed in tissues lacking PEG-NRs may be attributed to heat nonspecifically conducted from the device itself. In contrast, temperature elevations observed within the first minute of NIR exposure rose significantly steeper for tumors and liver in animals pretreated with PEG-NRs, while the trend was also increased but not significant for the intestine (Figure 4e−g). For tissues in the PEG-NR group, the maximum temperature changes for tumor, liver, and intestine were 6.27 °C ± 2.47 °C, 6.51 ± 1.47 °C, and 4.66 ± 2.49 °C, respectively (Figure 4h). Following PEG-NR photothermal heating, tissue sections were prepared to assess tissue viability and any resulting histological changes consistent with inflammatory or necrotic tissue damage. Importantly, normal tissue histology was observed for intestine, tumor, and liver by H&E staining (Figure 4i). Furthermore, Ki67-positive immunohistochemical staining confirmed that these tissues remained actively proliferative after photothermal heating (Figure 4i). Evidence of mild bleeding and coagulation at the device incision site, however, was noted in some animals investigated. These studies therefore establish that an implanted NIR device shown to selectively heat PEG-NR solutions in an *ex vivo* setting can likewise heat tissues containing PEG-NRs deep within the abdominal cavity while not inducing irreversible damage in these organs.

Plasmonic photothermal therapy and other modalities to heat tumors in the subablative range (*ca.* 41−45 °C) have been shown in subcutaneous models to alter the flow and permeability of tumor vessels and enhance accumulation of diffusion-limited therapeutic cargoes.[34−38] To investigate whether NIR irradiation from the implanted silica rod similarly drove accumulation of therapeutic cargoes in an orthotopic site,

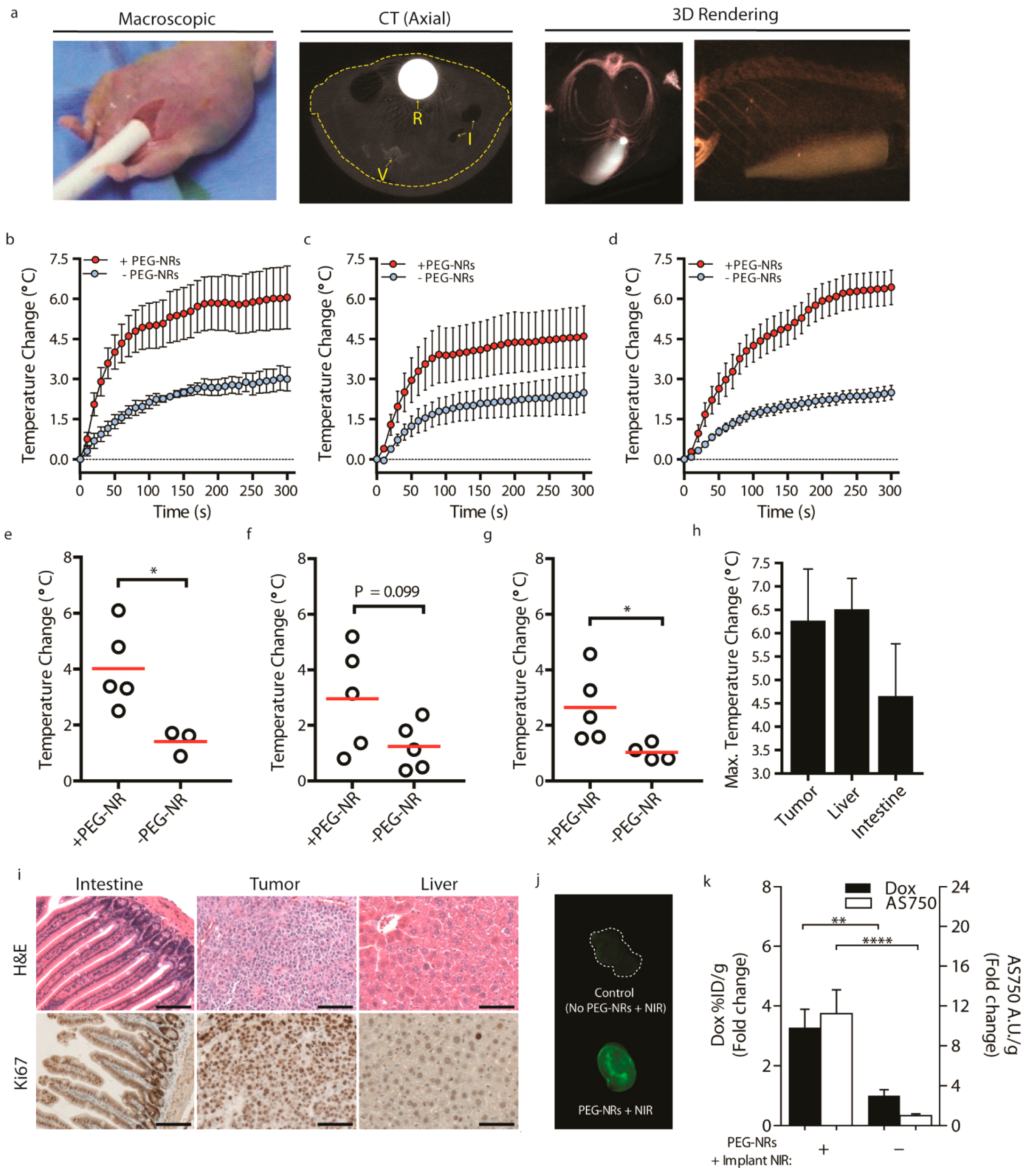

Figure 4. (a) Placement of implanted NIR device in a tumor-bearing animal shown macroscopically, by axial CT scan (R, rod; I, intestine; V, vertebrate; dashed line outlining body cavity), and 3D-rendered CT scanning. (b–d) Thermal profiling in the presence or absence of PEG-NRs in (b) ovarian tumors, (c) intestine, and (d) liver. (*n* = 3–5 per group). (e–g) Initial temperature change after 50 s of direct implanted NIR illumination in (e) tumors, (f) intestine, and (g) liver in PEG-NR-treated animals and controls. Red bar denotes mean value per group. (*n* = 3–5, **P* < 0.05, unpaired *t* test). (h) Maximal temperature change for tumor, liver, and intestine of PEG-NR-treated animals (*n* = 5 per tissue). Error bars, s.e.m. (i) Histology and Ki-67 immunohistochemical staining of tissues following PEG-NR therapy with implanted NIR device. Scale: 100 μm. (j) Whole-tumor fluorescence of AngioSPARK750 and (k) quantification of doxorubicin-loaded liposomes and AngioSPARK750 in tumor homogenates from tissues harvested 3 h after injection and PEG-NR/Implant NIR therapy or injection only. (*n* = 11–12 tumors, 3 animals per group, ***P* < 0.01,***P* < 0.0001, Mann–Whitney test) Error bars, s.e.m.**

tumors from NIR-treated and control animals were studied following administration of doxorubicin-loaded liposomes and the diagnostic imaging agent AngioSPARK750 (AS750; core diameter, 20–50 nm). We observed from prior studies that the lower third of the silica rod dispersed NIR light with high intensity, so this region was used to induce heating in tumors in this proof-of-principle study. Intraperitoneal tumors from the quadrant receiving NIR illumination and harvested 3 h after receiving AS750 and PEG-NR/implanted NIR heating demonstrated elevated macroscopic accumulation of AS750 (Figure 4j). Significantly elevated enhancements of 3.27 and 11.2 for doxorubicin-loaded liposomes and AS750, respectively, were measured in homogenized tumor samples from the PEG-NR/implanted NIR group relative to control tumors from animals receiving no PEG-NR/implanted NIR therapy (Figure 4k). These data suggest that plasmonic-based enhancement of therapeutic cargoes previously observed in subcutaneous tumor models[35] may also have utility for delivering cargoes to tumors in the abdominal cavity.

For *in vivo* thermographic studies, the liver and intestine were studied in addition to tumors for several reasons. First, previous work on the biodistribution of PEG-NRs has demonstrated a significant accumulation of PEG-NRs in the liver (~14% ID/g).[16] Because of its high PEG-NR concentration, large size, and proximity to orthotopic ovarian tumor nodules, the liver poses a challenge for tumor-specific photothermal heating in the abdominal cavity. The temperature elevations observed in the liver were anticipated, and, importantly, they relaxed to baseline temperatures within several minutes after the procedures. The intestine, while accumulating fewer PEG-NRs than the liver, has been shown to be sensitive to broad elevations in temperature. This has been observed most notably during investigations with heated chemotherapy administered directly into the abdominal cavity for ovarian cancer patients.[39] In this study, elevations in intestinal temperature were detected, but no tissue damage or proliferative defects were observed, and the thermal effects were more modest than in ovarian tumors or the liver, which is perhaps representative of differing PEG-NR concentrations within each of these tissues. A key advantage of PEG-NRs and plasmonic nanomaterials more generally is the ability to "sensitize" tumor tissue to incident NIR light relative to surrounding tissues containing fewer PEG-NRs. The ability to locally deposit heat in desired tissues using plasmonic nanomaterials stands in marked contrast to heated chemotherapy approaches which cause nonspecific temperature elevations throughout the entire abdominal cavity and have been associated with high morbidity and even mortality.[39] In the future, strategies to both shield nontumor, PEG-NR-rich tissues (e.g., liver) from implanted NIR light as well as spatially localize thermal gradients around PEG-NRs *via* pulsed laser sources could prove fruitful for mitigating any off-target effects.

CONCLUSIONS

Plasmonic nanomaterial-based therapies that generate localized heating within tumors hold great promise for future clinical interventions in oncology, but novel methods of delivering NIR light to deeply located and distributed solid tumors are needed for tumors that do not reside superficially beneath the skin. Here, to overcome the optical limitations of external NIR irradiation, we propose a possible alternative strategy using a biocompatible, implanted NIR illumination device and assess its functionality through computational modeling, *ex vivo* characterization, and *in vivo* thermographic profiling of orthotopic ovarian tumors. Ray tracing analysis in a simulated mouse model approximated the degree of NIR light penetration influenced by tissue scattering and absorption from two general device designs, providing a framework for selecting candidates for further study. These modeling predictions were validated and further refined by *ex vivo* fluence rate and thermographic measurements, as well as *in vivo* plasmonic photothermal heating of PEG-NR-containing ovarian tumors and nontumor tissues. We demonstrate that localized plasmonic heating of ovarian tumors by this method can enhance accumulation of diagnostic and therapeutic agents including doxorubicin liposomes in this orthotopic tumor model. In future studies, it will be valuable to investigate what therapeutic benefits may be attained in these deep-seated tumors and the degree to which they correlate with results obtained from related preclinical models as plasmonic nanomaterials advance closer to clinical use.

MATERIALS AND METHODS

Synthesis of PEG-NRs. Gold nanorods (GNRs) coated in PEG were prepared as described previously.[16,17] Briefly, 41 nm × 10 nm cetyltrimethylammonium (CTAB)-coated GNRs (Nanopartz) were concentrated ~100-fold by centrifugation at 15 000 rcf for 30 min, incubated with 5-kDa methyl-PEG-thiol (Laysan Bio, Inc.) to 100 μM, and dialyzed for at least 24 h against distilled, deionized water in 3500 MWCO Slide-A-Lyzer cassettes (Thermo Scientific). Dialyzed samples were washed in ultrapure water, filtered through 100-kDa filters (Millipore), and resuspended in PBS. PEG-NR solutions were stored at 4 °C.

Device Design and Construction. Implanted devices consisted of silica rods and fiber optic meshes (Rogers Sciences, Inc.). Silica rods were treated by an optomechanical scoring process to create varying illumination patterns and light-dispersive coatings. Light emission was incoherent with an exitance of $\sim 2\pi$ steradians at each illumination surface. Fiber optic meshes were encased in medical-grade silicone to provide adhesion, flexibility, and biocompatibility. Meshes were treated in an array format by an optomechanical scoring process to allow approximately uniform light emission from the top surface.

Computational Modeling. An approximate anatomical model of the mouse was developed including liver, intestine, kidney, stomach, spleen, lungs, vertebrae, and skin using a nude mouse (female) atlas as a guide (Xenogen). Tissue layers were assigned indices of refraction, scattering coefficients, and absorption coefficients. Implanted NIR devices (silica rod, flexible mesh) were simulated in this three-dimensional anatomical model using Zemax and TracePro software. Each simulation performed consisted of 1×10^4 distinct ray tracings. NIR illumination from the silica rod was modeled as 1×10^4 ray tracings across the device's entire length and diameter, while illumination from the fiber optic mesh was modeled as 1×10^4 ray tracings emitted from the top and bottom surfaces of the mesh. The surfaces for both devices were modeled with a lambertian reflectance profile (1 W, 808 nm).

Fluence Rate Measurements. Implanted NIR devices were directly coupled to an 810 nm continuous diode laser source (Visotek) through an SMA-threaded glass fiber optic cable (0.4 mm diameter). Fluence rate measurements were recorded on an optical power and energy meter with an S121C silicon photodiode power sensor (400–1100 nm, 500 mW) (Thorlabs).

Measurements were obtained at 808 nm at multiple distances and input currents.

***Ex vivo* Thermographic Profiling.** Solutions of PEG-NRs (0, 1, 10, and 100 μg/mL) were irradiated by implanted NIR devices for 3 min. Maximal surface temperatures of PEG-NR solutions were monitored continuously by infrared thermography (Thermacam S60, FLIR). Each concentration of PEG-NRs was identically exposed to the 810 nm laser illumination. All conditions reported were measured in triplicate.

***In Vivo* Imaging.** All animal studies were approved by the MIT Committee on Animal Care. Computed tomographic (CT) imaging on animals with implanted NIR devices was performed on an eXplore CT120-whole mouse MicroCT system (GE Healthcare). Image analysis for anatomic measurements and three-dimensional rendering was performed with MicroView software (GE Healthcare).

***In Vivo* Thermographic Profiling.** Female NCR nude mice at ~4 weeks of age (Taconic) received an intraperitoneal injection of ~5×10^5 OVCAR8 human ovarian cancer cells expressing firefly luciferase. At 4–6 weeks following implantation, the establishment of tumors was confirmed on the whole-animal IVIS spectrum-bioluminescent and fluorescent imaging system (Xenogen). Tumor-bearing animals received either an intravenous injection of PEG-NRs (100 μL; ~14 mg Au/kg) or no injection for the control group; after vascular clearance (~48 h), animals were anesthetized and a midline incision through the skin and abdominal wall was made for implantation of the silica rod NIR device under study. To assess tissue-specific heating properties, the implanted NIR device was independently positioned in proximity to the liver, intestine, and ovarian tumors within the abdominal cavity. K-type fiberglass thermocouples (National Instruments) were placed adjacent to each tissue and equidistantly from the NIR device (ca. 0.3–0.5 cm) to minimize nonspecific direct heating effects from the device. Implanted devices were connected *via* fiber optic cable to a continuous 810 nm laser source (Visotek) during a five minute heating period per tissue. Thermocouple temperature signals were integrated on a portable DAQ thermocouple module (NI USB-9211A, National Instruments) and recorded at 2 Hz with NI-DAQmx and LabView software during the five minute heating window. Thermographic profiles were assembled and statistically analyzed with Prism 5 software (GraphPad).

Histology. Harvested tissues were fixed in 4% paraformaldehyde overnight at 4 °C prior to paraffin embedding. Standard hematoxylin and eosin (H&E) staining was performed on sections of tumor, liver, and intestine. Immunohistochemical staining for the cell proliferation protein Ki67 was performed with primary antibody rabbit antihuman Ki67 (1:100, EMD Millipore). IHC with antigen retrieval was performed on the LabVision Autostainer 360 Immunohistochemical Stainer (Thermo Scientific).

***In Vivo* Quantification of Cargo.** Tumor-bearing animals received an intravenous coinjection of doxorubicin-loaded liposomes (8 mg Dox/kg) and AngioSPARK750 (100 μL in PBS) (Perkin-Elmer). The silica rod was implanted as described and positioned in proximity to multiple tumor nodules within a specified quadrant of the abdomen. Each animal received continuous NIR light irradiation (810 nm) for 30 min and the abdominal wall and skin were sutured prior to recovery. Three hours after the procedure, tumors were harvested and AS750 fluorescence within whole tumors was imaged on an NIR imaging system (LICOR Odyssey). Tumors were weighed and homogenized in 1.0 mL of extraction buffer (70% EtOH, 0.3 N HCl) using an automated tissue homogenizer (gentleMACS Octo Dissociator, Miltenyi Biotec). Supernatants were measured on LICOR platform for AS750 and a fluorescence microplate reader (Molecular Devices, SpectraMAX GeminiEM) for doxorubicin fluorescence. For each group, the fluorescence of 12 individual tumor supernatants obtained from three mice per group was normalized by tissue weight prior to analysis.

Conflict of Interest: The authors declare the following competing financial interest(s): G.S.R. and S.H. hold intellectual property related to the illumination sources and have formed a start-up entity to facilitate commercialization.

Acknowledgment. The authors wish to dedicate this paper to the memory of Officer Sean Collier, for his caring service to the MIT community and for his sacrifice. The authors would like to acknowledge H. Fleming and K. Reddy for their helpful suggestions on the manuscript. The authors also acknowledge S. Malstrom from the Koch Institute Applied Therapeutics and Whole Animal Imaging (ATWAI) Core Facility, as well as the Koch Institute Histology Core facility. A.F.B. acknowledges support from the NIH/Medical Scientist Training Program and Biophysics Program at Harvard University. S.B. is an HHMI investigator.

Supporting Information Available: Modeling parameters and schematics for NIR light simulations, *ex vivo* thermography of several implanted devices, and anatomic measurements of device implanted within the abdominal cavity. This material is available free of charge *via* the Internet at http://pubs.acs.org.

REFERENCES AND NOTES

1. Huang, X. H.; Jain, P. K.; El-Sayed, I. H.; El-Sayed, M. A. Gold Nanoparticles: Interesting Optical Properties and Recent Applications in Cancer Diagnostics and Therapy. *Nanomedicine* **2007**, *2*, 681–693.
2. Huang, X. H.; Neretina, S.; El-Sayed, M. A. Gold Nanorods: From Synthesis and Properties to Biological and Biomedical Applications. *Adv. Mater.* **2009**, *21*, 4880–4910.
3. Jain, P. K.; Huang, X. H.; El-Sayed, I. H.; El-Sayed, M. A. Noble Metals on the Nanoscale: Optical and Photothermal Properties and Some Applications in Imaging, Sensing, Biology, and Medicine. *Acc. Chem. Res.* **2008**, *41*, 1578–1586.
4. Pissuwan, D.; Valenzuela, S. M.; Cortie, M. B. Therapeutic Possibilities of Plasmonically Heated Gold Nanoparticles. *Trends Biotechnol.* **2006**, *24*, 62–67.
5. Mieszawska, A. J.; Mulder, W. J. M.; Fayad, Z. A.; Cormode, D. P. Multifunctional Gold Nanoparticles for Diagnosis and Therapy of Disease. *Mol. Pharm.* **2013**, *10*, 831–847.
6. Hutter, E.; Fendler, J. H. Exploitation of Localized Surface Plasmon Resonance. *Adv. Mater.* **2004**, *16*, 1685–1706.
7. El-Sayed, I. H.; Huang, X.; El-Sayed, M. A. Surface Plasmon Resonance Scattering and Absorption of Anti-EGFR Antibody Conjugated Gold Nanoparticles in Cancer Diagnostics: Applications in Oral Cancer. *Nano Lett.* **2005**, *5*, 829–834.
8. Raschke, G.; Kowarik, S.; Franzl, T.; Sonnichsen, C.; Klar, T. A.; Feldmann, J.; Nichtl, A.; Kurzinger, K. Biomolecular Recognition Based on Single Gold Nanoparticle Light Scattering. *Nano Lett.* **2003**, *3*, 935–938.
9. Sonnichsen, C.; Alivisatos, A. P. Gold Nanorods as Novel Nonbleaching Plasmon-Based Orientation Sensors for Polarized Single-Particle Microscopy. *Nano Lett.* **2005**, *5*, 301–304.
10. Aslan, K.; Holley, P.; Davies, L.; Lakowicz, J. R.; Geddes, C. D. Angular-Ratiometric Plasmon-Resonance Based Light Scattering for Bioaffinity Sensing. *J. Am. Chem. Soc.* **2005**, *127*, 12115–12121.
11. Aslan, K.; Lakowicz, J. R.; Geddes, C. D. Nanogold Plasmon Resonance-Based Glucose Sensing. 2. Wavelength-Ratiometric Resonance Light Scattering. *Anal. Chem.* **2005**, *77*, 2007–2014.
12. Haes, A. J.; Chang, L.; Klein, W. L.; Van Duyne, R. P. Detection of a Biomarker for Alzheimer's Disease from Synthetic and Clinical Samples Using a Nanoscale Optical Biosensor. *J. Am. Chem. Soc.* **2005**, *127*, 2264–2271.
13. Hirsch, L. R.; Stafford, R. J.; Bankson, J. A.; Sershen, S. R.; Rivera, B.; Price, R. E.; Hazle, J. D.; Halas, N. J.; West, J. L. Nanoshell-Mediated Near-Infrared Thermal Therapy of Tumors under Magnetic Resonance Guidance. *Proc. Natl. Acad. Sci. U.S.A.* **2003**, *100*, 13549–13554.
14. Pitsillides, C. M.; Joe, E. K.; Wei, X. B.; Anderson, R. R.; Lin, C. P. Selective Cell Targeting with Light-Absorbing Microparticles and Nanoparticles. *Biophys. J.* **2003**, *84*, 4023–4032.
15. Hainfeld, J. F.; Slatkin, D. N.; Smilowitz, H. M. The Use of Gold Nanoparticles To Enhance Radiotherapy in Mice. *Phys Med Biol* **2004**, *49*, N309–N315.
16. von Maltzahn, G.; Park, J. H.; Agrawal, A.; Bandaru, N. K.; Das, S. K.; Sailor, M. J.; Bhatia, S. N. Computationally Guided

Photothermal Tumor Therapy Using Long-Circulating Gold Nanorod Antennas. *Cancer Res.* **2009**, *69*, 3892–3900.

17. Lin, K. Y.; Bagley, A. F.; Zhang, A. Y.; Karl, D. L.; Yoon, S. S.; Bhatia, S. N. Gold Nanorod Photothermal Therapy in a Genetically Engineered Mouse Model of Soft Tissue Sarcoma. *Nano LIFE* **2010**, *1*, 277–287.
18. Bartczak, D.; Muskens, O. L.; Millar, T. M.; Sanchez-Elsner, T.; Kanaras, A. G. Laser-Induced Damage and Recovery of Plasmonically Targeted Human Endothelial Cells. *Nano Lett.* **2011**, *11*, 1358–1363.
19. Elghanian, R.; Storhoff, J. J.; Mucic, R. C.; Letsinger, R. L.; Mirkin, C. A. Selective Colorimetric Detection of Polynucleotides Based on the Distance-Dependent Optical Properties of Gold Nanoparticles. *Science* **1997**, *277*, 1078–1081.
20. Jackson, J. B.; Westcott, S. L.; Hirsch, L. R.; West, J. L.; Halas, N. J. Controlling the Surface Enhanced Raman Effect *via* the Nanoshell Geometry. *Appl. Phys. Lett.* **2003**, *82*, 257–259.
21. Qian, X.; Peng, X.-H.; Ansari, D. O.; Yin-Goen, Q.; Chen, G. Z.; Shin, D. M.; Yang, L.; Young, A. N.; Wang, M. D.; Nie, S. *In Vivo* Tumor Targeting and Spectroscopic Detection with Surface-Enhanced Raman Nanoparticle Tags. *Nat. Biotechnol.* **2008**, *26*, 83–90.
22. O'Neal, D. P.; Leon, R. H.; Naomi, J. H.; Payne, J. D.; Jennifer, L. W. Photo-thermal Tumor Ablation in Mice Using Near Infrared-Absorbing Nanoparticles. *Cancer Lett.* **2004**, *209*, 171–176.
23. von Maltzahn, G.; Centrone, A.; Park, J.-H.; Ramanathan, R.; Sailor, M. J.; Hatton, T. A.; Bhatia, S. N. SERS-Coded Gold Nanorods as a Multifunctional Platform for Densely Multiplexed Near-Infrared Imaging and Photothermal Heating. *Adv. Mater.* **2009**, *21*, 3175–3180.
24. Dickerson, B. E.; Erik, C. D.; Xiaohua, H.; Ivan, H. E.-S.; Hunghao, C.; Sujatha, P.; John, F. M.; Mostafa, A. E.-S. Gold Nanorod Assisted Near-Infrared Plasmonic Photothermal Therapy (PPTT) of Squamous Cell Carcinoma in Mice. *Cancer Lett.* **2008**, *269*, 57–66.
25. Wilson, B. C.; Jacques, S. L. Optical Reflectance and Transmittance of Tissues—Principles and Applications. *IEEE J. Quantum Elect.* **1990**, *26*, 2186–2199.
26. Star, W. M. Light Dosimetry *in Vivo*. *Phys. Med. Biol.* **1997**, *42*, 763–787.
27. Panjehpour, M.; Overholt, B. F.; Haydek, J. M. Light Sources and Delivery Devices for Photodynamic Therapy in the Gastrointestinal Tract. *Gastrointest. Endosc. Clin. North Am.* **2000**, *10*, 513–532.
28. van den Bergh, H. On the Evolution of Some Endoscopic Light Delivery Systems for Photodynamic Therapy. *Endoscopy* **1998**, *30*, 392–407.
29. Muschter, R.; Hessel, S.; Hofstetter, A.; Keiditsch, E.; Rothenberger, K. H.; Schneede, P.; Frank, F. Interstitial Laser Coagulation of Benign Prostatic Hyperplasia. *Urol. A* **1993**, *32*, 273–281.
30. Ascher, P. W.; Justich, E.; Schrottner, O. A New Surgical but Less Invasive Treatment of Central Brain Tumours: Preliminary Report. *Acta Neurochir. Suppl. (Wien)* **1991**, *52*, 78–80.
31. Svaasand, L. O.; Gomer, C. J.; Profio, A. E. Laser-Induced Hyperthermia of Ocular Tumors. *Appl. Opt.* **1989**, *28*, 2280–2287.
32. Klingenberg, M.; Bohris, C.; Niemz, M. H.; Bille, J. F.; Kurek, R.; Wallwiener, D. Multifibre Application in Laser-Induced Interstitial Thermotherapy Under On-Line MR Control. *Laser Med. Sci.* **2000**, *15*, 6–14.
33. Niemz, M. H. *Laser-Tissue Interactions: Fundamentals and Applications*, 3rd, enlarged ed.; Springer: Berlin, New York, 2004; 305 p.
34. Kong, G.; Braun, R. D.; Dewhirst, M. W. Characterization of the Effect of Hyperthermia on Nanoparticle Extravasation from Tumor Vasculature. *Cancer Res.* **2001**, *61*, 3027–3032.
35. Park, J. H.; von Maltzahn, G.; Xu, M. J.; Fogal, V.; Kotamraju, V. R.; Ruoslahti, E.; Bhatia, S. N.; Sailor, M. J. Cooperative Nanomaterial System to Sensitize, Target, and Treat Tumors. *Proc. Natl. Acad. Sci. U.S.A.* **2010**, *107*, 981–986.
36. Dudar, T. E.; Jain, R. K. Differential Response of Normal and Tumor Microcirculation to Hyperthermia. *Cancer Res.* **1984**, *44*, 605–612.
37. Jain, R. K. Vascular and Interstitial Barriers to Delivery of Therapeutic Agents in Tumors. *Cancer Metast. Rev.* **1990**, *9*, 253–266.
38. Jain, R. K. Transport of Macromolecules in Tumor Microcirculation. *Biotechnol. Prog.* **1985**, *1*, 81–94.
39. Witkamp, A. J.; de Bree, E.; Van Goethem, R.; Zoetmulder, F. A. Rationale and Techniques of Intra-operative Hyperthermic Intraperitoneal Chemotherapy. *Cancer Treat. Rev.* **2001**, *27*, 365–374.

Supporting Information

This supporting information includes:

Fig. S1. Anatomic models of abdominal cavity used in fluence rate simulations.
Fig. S2. *Ex vivo* thermographic profiles for implantable devices.
Fig. S3. Measured distances between implanted device and anatomic landmarks.
Fig. S4. Measured distances between implanted device and thermocouple.
Table 1. Optical coefficients for modeling simulations

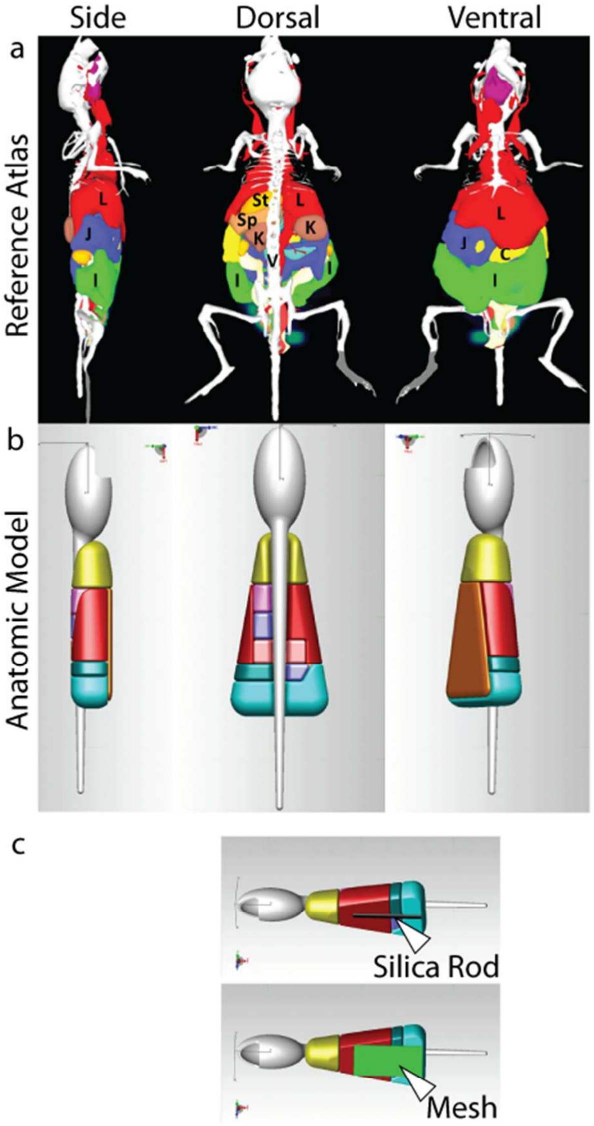

Figure S1. Anatomic models of abdominal cavity used in fluence rate simulations. (a) Reference atlas overlay on tumor-bearing, female nude mouse from side, dorsal, and ventral orientations. (L, liver; J, jejunum (intestine); C, cecum (intestine); I, ileum (intestine); St, stomach; Sp, spleen; K, kidney; V, vertebral body) (b) Approximate anatomic model developed for simulations. Each tissue assigned optical coefficients for refraction, scattering, and absorption. (c) Models depicting implanted silica rod (top) and fiber optic mesh (bottom).

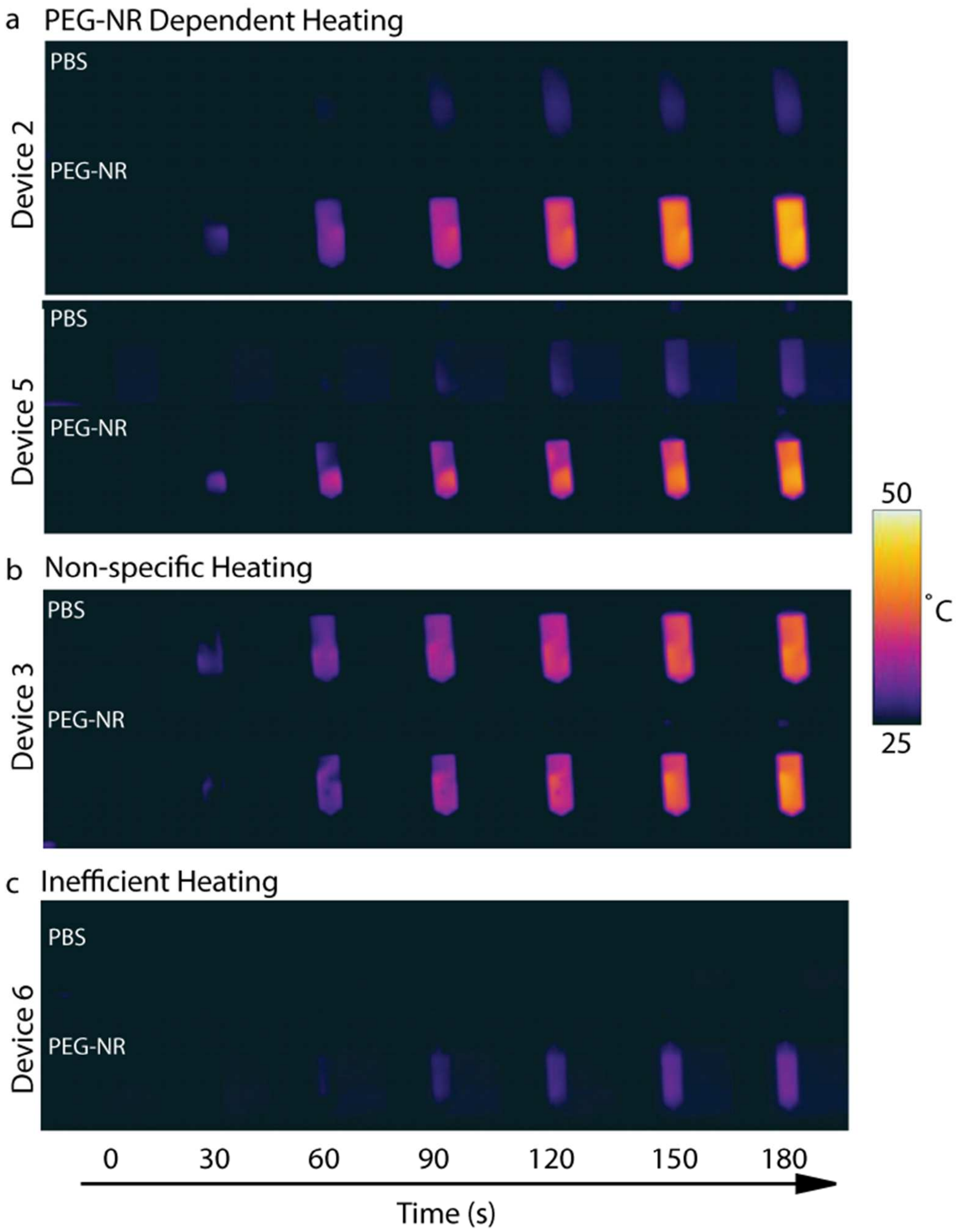

Figure S2. *Ex vivo* thermographic profiles for implantable devices. Images show devices 2, 3, 5, and 6 in solutions of PEG-NRs or control PBS. (a) Devices 2 and 5 demonstrate PEG-NR-dependent heating; (b) Device 3 demonstrates non-specific heating; (c) and Device 6 demonstrates inefficient heating.

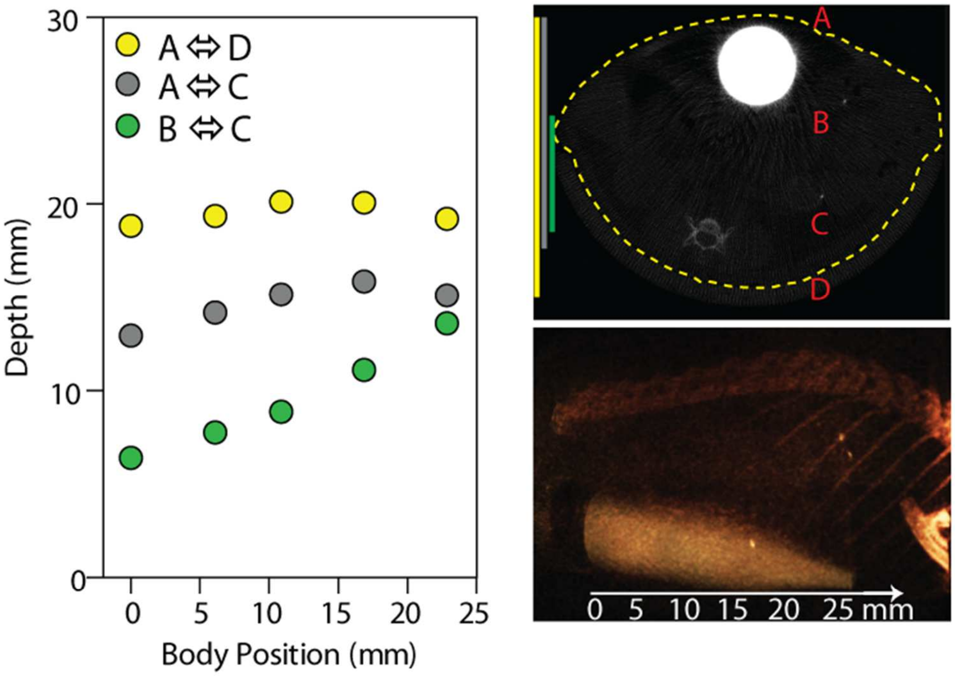

Figure S3. Measured distances between implanted device and anatomic landmarks. Landmarks include vertebrae, ventral and dorsal surfaces measured at multiple locations along body length by microCT image analysis.

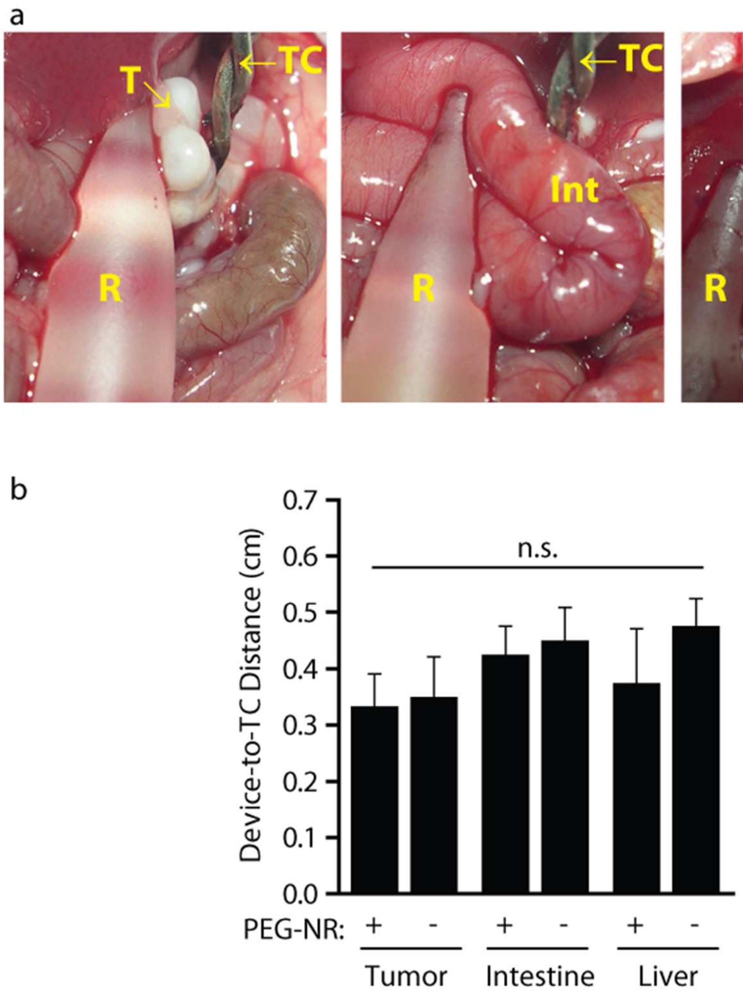

Figure S4. Measured distances between implanted device and thermocouple. (a) Representative images of implanted glass rod device (R), ovarian tumors (T), intestine (Int), liver (L), and thermocouple (TC). (b) Distances between implanted glass rod device and thermocouples for each tissue in presence or absence of PEG-NRs. (one-way ANOVA and Tukey's post test, *n*=4 for liver, intestine; *n*=2-3 for tumors). Error bars, s.d.

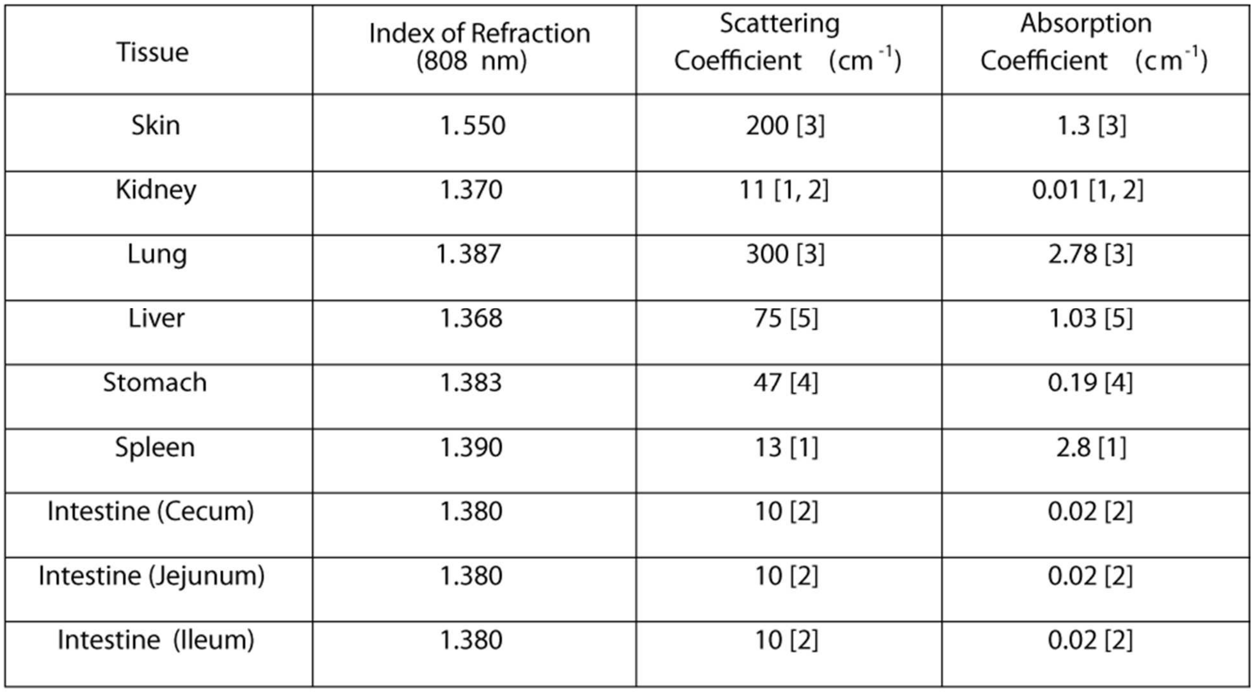

Tissue	Index of Refraction (808 nm)	Scattering Coefficient (cm^{-1})	Absorption Coefficient (cm^{-1})
Skin	1.550	200 [3]	1.3 [3]
Kidney	1.370	11 [1, 2]	0.01 [1, 2]
Lung	1.387	300 [3]	2.78 [3]
Liver	1.368	75 [5]	1.03 [5]
Stomach	1.383	47 [4]	0.19 [4]
Spleen	1.390	13 [1]	2.8 [1]
Intestine (Cecum)	1.380	10 [2]	0.02 [2]
Intestine (Jejunum)	1.380	10 [2]	0.02 [2]
Intestine (Ileum)	1.380	10 [2]	0.02 [2]

Table 1. Optical Coefficients for Modeling Simulations

1. Srinivasan, R.; Kumar, D.; Singh, M. Optical Tissue-Equivalent Phantoms for Medical Imaging. *Trends Biomater.* **2002**, *15*, 42-47.
2. Soloneno, M.; Cheung, R.; Busch, T.M.; Kachur, A.; Griffin, G.M.; Vulcan, T.; Zhu, T.C.; Wang, H.W.; Hahn, S.M.; Yodh, A.G. *In Vivo* Reflectance Measurements of Optical Properties, Blood Oxygenation, and Motexafin Lutetium Uptake in Canine Large Bowels, Kidneys, and Prostates. *Phys Med Biol* **2002**, *47*, 857-873.
3. Cheong, W.F.; Prahl, S.A.; Welch, A.J. A Review of the Optical Properties of Biological Tissues. *IEEE J. Quantum Electron.* **1990**, *26*, 2166-2185.
4. Bashkatov, A.N.; Genina, E.A.; Kochubey, V.I.; Gavrilova, A.A.; Kapralov, S.V.; Grishaev, V.A.; Tuchin, V.V. Optical Properties of Human Stomach Mucosa in the Spectral Range from 400 to 2000nm. *Med. Laser App.* **2007**, *22*, 95-104.
5. Ullah, H.; Atif, S.; Firdous, M.S.; Mehmood, M.; Ikram, C.; Kurachi, C.; Grecco, C.; Nicolodelli, G.; Bagnato, V.S. Femtosecond Light Distribution at Skin and Liver of Rats: Analysis for Use in Optical Diagnostics. *Laser Phys. Lett.* **2010**, *7*, 889-898.